

An *XMM–Newton* view of M101 – III. Diffuse X-ray emission

R. S. Warwick,¹[★] L. P. Jenkins,^{1,2} A. M. Read,¹ T. P. Roberts^{1,3} and R. A. Owen¹

¹ *X-ray & Observational Astronomy Group, Department of Physics & Astronomy, University of Leicester, University Road, Leicester LE1 7RH*

² *Laboratory for X-ray Astrophysics, NASA Goddard Space Flight Centre, Greenbelt, MD 20771, USA*

³ *Department of Physics, Durham University, South Road, Durham DH1 3LE*

Accepted 2007 January 30. Received 2007 January 23; in original form 2006 November 20

ABSTRACT

We present a study of the X-ray properties of the nearby face-on Scd spiral galaxy M101 based on recent *XMM–Newton* observations. In this third and final paper in the present series, we focus on the spatial and spectral properties of the residual emission, after excluding bright X-ray sources with $L_X > 10^{37}$ erg s^{−1}. Within a central region of radius 10 arcmin (21 kpc), the X-ray emission broadly traces the pattern of the spiral arms, establishing a strong link with recent star formation, but it also exhibits a radial scalelength of ≈ 2.6 arcmin (5.4 kpc) consistent with optical data. We estimate the soft X-ray luminosity within the central 5 arcmin (10.5 kpc) region to be $L_X \approx 2.1 \times 10^{39}$ erg s^{−1} (0.5–2 keV), the bulk of which appears to originate as diffuse emission. We find a two-temperature thermal model best fits the spectral data with derived temperatures of $0.20^{+0.01}_{-0.01}$ and $0.68^{+0.06}_{-0.04}$ keV which are very typical of the diffuse components seen in other normal and starburst galaxies. More detailed investigation of the X-ray morphology reveals a strong correlation with images recorded in the far-ultraviolet through to V band, with the best match being with the U band. We interpret these results in terms of a clumpy thin-disc component which traces the spiral arms of M101 plus an extended lower halo component with large filling factor.

Key words: galaxies: individual: M101 – galaxies: spiral – X-rays: galaxies – X-rays: ISM.

1 INTRODUCTION

The hot ($T \sim 10^6$ K), X-ray emitting plasma observed in the disc of our Galaxy is an important factor when considering the energy balance and enrichment of the interstellar medium (ISM). Energized by the winds of young massive stars and supernovae, its properties relate to the supernova rate, the evolution of supernova remnants (SNRs) and the impact of young star clusters on their environment. In normal spiral galaxies like the Milky Way, hot gas produced by multiple supernova explosions may escape from the disc via galactic fountains and/or chimneys (Shapiro & Field 1976; Bregman 1980; Norman & Ikeuchi 1989) resulting in a dynamic corona that is bound to the galaxy. This gas then cools, condenses and falls back to the disc, possibly as high-velocity clouds (Bregman 1980). In contrast, the extremely high star formation rates in starburst galaxies give rise to hotter ($T \gtrsim 10^7$ K) large-scale metal-rich outflows from the starburst regions in the form of ‘superwinds’ (e.g. Heckman, Armus & Miley 1990). Such superwinds are energetic enough to fully escape the influence of the galaxy and are potentially important for the enrichment and heating of the intergalactic medium (e.g. Martin, Kobulnicky & Heckman 2003).

Unfortunately, the opacity of the Galactic plane to soft X-rays greatly complicates the study of the extent, physical properties and filling factor of the X-ray emitting plasma in our own Galaxy. However, observations of nearby spiral galaxies with configurations ranging from face-on to edge-on can circumvent many of the problems inherent in studies of the Milky Way. The *Einstein* observatory provided the first detection of ultrahot outflows from the discs of edge-on starburst galaxies (Watson, Stanger & Griffiths 1984), although only upper limits were obtained on the diffuse emission produced in the discs of normal spiral galaxies (Bregman & Glassgold 1982; McCammon & Sanders 1984). The improved throughput and spatial resolution of subsequent *ROSAT* Position Sensitive Proportional Counter (PSPC)/High Resolution Imager (HRI) observations revealed unambiguous evidence for truly diffuse emission in spiral galaxies (Cui et al. 1996; Read, Ponman & Strickland 1997). More recently, diffuse structures have been observed with the *XMM–Newton* and *Chandra* observatories in samples of both edge-on (Pietsch et al. 2001; Stevens, Read & Bravo-Guerrero 2003; Strickland et al. 2004a,b) and face-on spiral galaxies (Kuntz et al. 2003; Tyler et al. 2004). In the face-on systems, diffuse X-rays were found to correlate with the nuclear regions, trace recent star formation within the spiral arms and correlate spatially with H α and mid-infrared emission (Tyler et al. 2004). In the survey of edge-on systems by Strickland et al. (2004a,b), extraplanar diffuse emission was detected in all starburst galaxies and one normal spiral

[★]E-mail: rsw@star.le.ac.uk

Table 1. Details of the three *XMM–Newton* observations of M101.

No.	Observation ID	Date (yyyy-mm-dd)	Filter	Pointing co-ordinates		Useful exposure (ks)	
				RA (J2000)	Dec. (J2000)	pn	MOS
1	0104260101	2002-06-04	Medium	14 ^h 03 ^m 10 ^s .0	+54° 20′24″	25.7	36.7
2	0164560701	2004-07-23	Medium	14 ^h 03 ^m 32 ^s .3	+54° 21′03″	26.2	28.9
3	0212480201	2005-01-08	Thin	14 ^h 03 ^m 32 ^s .7	+54° 21′02″	27.7	25.8

galaxy, the extent of which correlated with estimates of the rate of star formation within the discs.

Clearly, if the purpose is to image the X-ray emission over a wide bandwidth, one should preferentially select galaxies in directions where the line-of-sight Galactic hydrogen column density is low. In this context, the Scd supergiant spiral M101 (NGC 5457), for which $N_{\text{H}} = 1.1 \times 10^{20} \text{ cm}^{-2}$ (Dickey & Lockman 1990), is an ideal candidate for a face-on study. A diffuse X-ray component was first hinted at in the central regions of M101 with *Einstein* at energies in the range 0.2–1.5 keV (McCammon & Sanders 1984; Trinchieri, Fabbiano & Romaine 1990). Subsequent *ROSAT* PSPC observations (Snowden & Pietsch 1995) revealed extensive diffuse X-ray emission in the 0.1–1 keV band, corresponding to thermal emission in the temperature range $1\text{--}3 \times 10^6 \text{ K}$. The dominant soft component was spatially peaked towards the centre of the galaxy but could also be traced out to a radius of at least 7 arcmin (15 kpc at a distance of 7.2 Mpc). It was argued that this soft emission could not originate solely in the disc as this would require a filling factor greater than unity. After correcting for absorption intrinsic to M101, the total diffuse luminosity was estimated to be at least $10^{40} \text{ erg s}^{-1}$.

In the *ROSAT* HRI study of Wang, Immler & Pietsch (1999), low surface-brightness X-ray emission was detected both in the central region of M101 and in the vicinity of bright H II regions in the spiral arms of the galaxy. The improved spatial resolution of the HRI (~ 5 arcsec) allowed the detection and subtraction of point sources down to a luminosity of $4 \times 10^{37} \text{ erg s}^{-1}$, after which the total 0.5–2 keV luminosity of the residual emission within a radius of 12 arcmin was estimated to be $9 \times 10^{39} \text{ erg s}^{-1}$. These authors agreed with Snowden & Pietsch (1995) that faint discrete X-ray sources were likely to account for only a fraction of the observed flux, implying that the bulk of the soft emission is truly diffuse in nature. The X-ray spectra of the emission in the central region from both the *ROSAT* PSPC and *ASCA* GIS were fitted simultaneously, yielding a soft thermal component with a temperature of $kT \sim 0.2 \text{ keV}$, plus a hard power-law continuum most plausibly explained as the integrated emission of the population of hard X-ray binary sources (XRBs) in M101.

Further progress was made in the *Chandra* study of Kuntz et al. (2003), using data from the 8 arcmin² ACIS-S3 chip from the first ~ 100 ks *Chandra* observation of M101. The superb spatial resolution of *Chandra* allowed the removal of point sources down to luminosities of $\sim 10^{36} \text{ erg s}^{-1}$, leaving residual emission of luminosity $2.3 \times 10^{39} \text{ erg s}^{-1}$ in the 0.45–1.0 keV band, 16 per cent of which was estimated to come from unresolved XRBs and dwarf stars. The bulk of the soft emission was found to trace the spiral arms and was also spatially correlated with H α and far-ultraviolet (FUV) emission, physically linking the soft X-ray emission to regions of on-going star formation. The X-ray spectrum of the diffuse emission was well described by a two-temperature thermal plasma with $kT = 0.2/0.75 \text{ keV}$, with a large covering factor implying that a significant fraction of the softest component originates in the halo of M101.

This is the third in a series of papers reporting the results of *XMM–Newton* observations of M101. In Jenkins et al. (2004a) (hereafter Paper I), the spectral and timing properties of the brightest X-ray sources were investigated, whereas in Jenkins et al. (2005b) (hereafter Paper II) we reported on the full catalogue of X-ray sources detected in M101 by *XMM–Newton*. In the current paper, we focus on the morphology and spectral properties of the ‘diffuse’ X-ray component in this galaxy. The structure of this paper is as follows. First, we describe the *XMM–Newton* observations and the methods used to construct images and spectra of the residual emission after the exclusion of bright discrete sources (Section 2). Next, we investigate the likely composition, spectral properties and spatial morphology of this residual emission (Section 3). We then go on to discuss the implications of our results (Section 4) and, finally, provide a brief summary of our conclusions (Section 5). Throughout this paper, we assume a distance to M101 of 7.2 Mpc (Stetson et al. 1998), implying that an angular scale of 1 arcmin corresponds to a linear extent of 2.09 kpc in M101.

2 OBSERVATIONS AND DATA REDUCTION

Three *XMM–Newton* EPIC observations have been made of M101 as summarized in Table 1. Our earlier analysis of the point source population in M101, presented in Papers I and II of this series, utilized only the first observation performed in 2002. However, for this paper, we have taken advantage of two additional observations carried out by *XMM–Newton* in 2004/2005 as a Target of Opportunity (TOO) programme to follow up the outburst of the ultraluminous supersoft X-ray source J140332.3+542103 (see Kong, Di Stefano & Yuan 2004; Mukai et al. 2005). The first *XMM–Newton* observation was targeted at the nucleus of the galaxy with the result that the 30 arcmin diameter field-of-view of the EPIC cameras encompassed the full 28.8 arcmin (D_{25}) extent of M101 (de Vaucouleurs et al. 1991). In the second and third observations, the source J140332.3+542103 was placed on axis, resulting in a 3.3 arcmin eastward offset of the field-of-view with respect to the first observation.

All data sets were screened for periods of high background by accumulating full field 10–15 keV light curves. MOS data were excluded during periods when the 10–15 keV count rate exceeded 0.3 ct s^{-1} , and the pn data were similarly screened when the pn count rate exceeded 3 ct s^{-1} (except in Observation 1, which was more heavily contaminated by flaring, where the pn threshold was set at 0.9 ct s^{-1}). For the subsequent image and spectral analysis, single- and double-pixel events were selected for the pn (Pattern 0–4), whereas single to quadruple events (Pattern 0–12) were utilized in the case of the MOS data.

2.1 Image processing and point source subtraction

To study the morphology of the diffuse component, pn and MOS images and associated exposure maps were created for each observation in three energy bands: soft (0.3–1 keV), medium (1–2 keV)

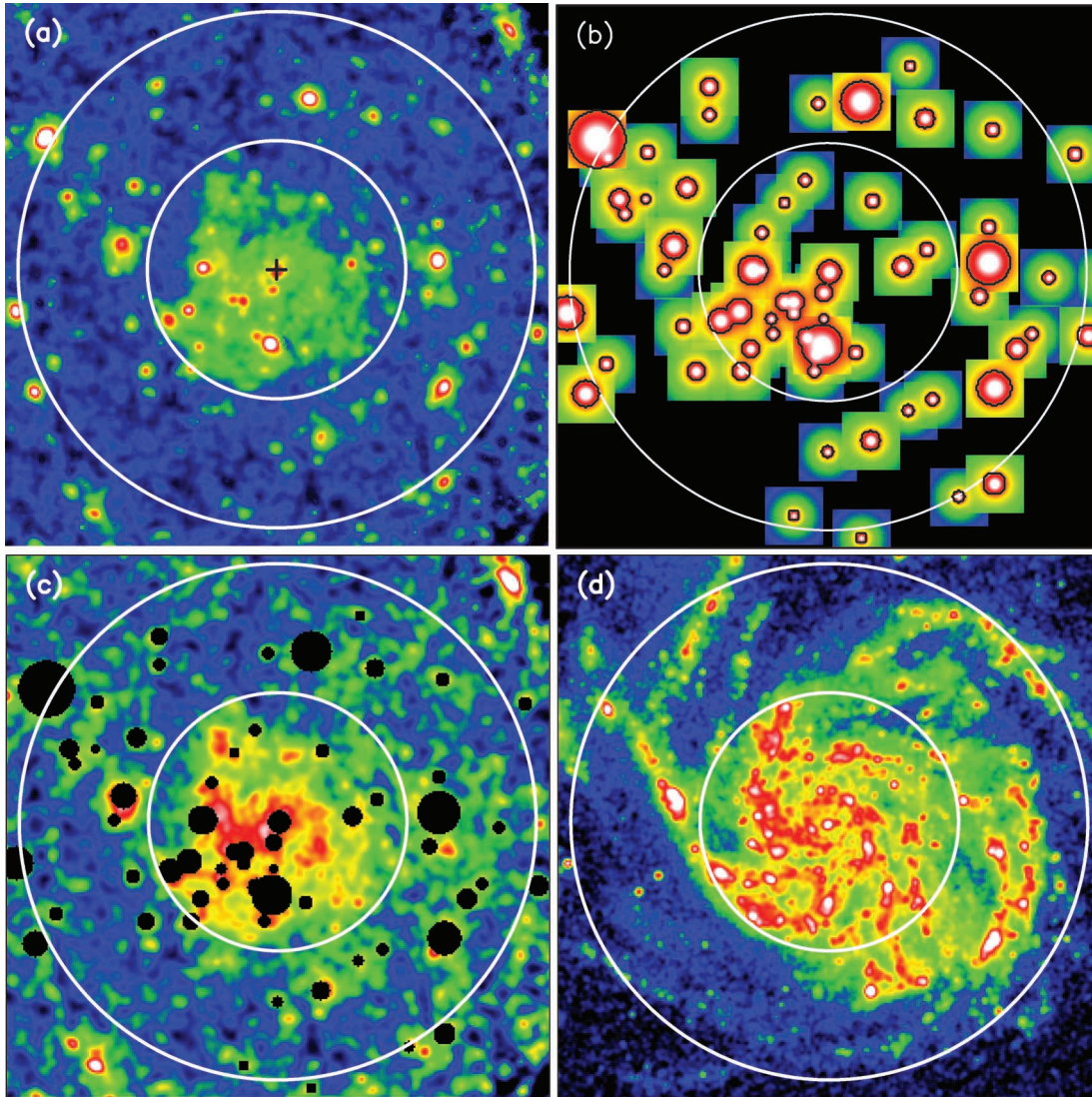


Figure 1. (a) *XMM–Newton* soft-band (0.3–1 keV) image of the central 20 arcmin of M101. This flat-fielded image is constructed using pn and MOS data from the three *XMM–Newton* observations. The amplitude scaling is logarithmic with a dynamic range (maximum to minimum in the colour table) of 50. The position of the optical nucleus of M101 is marked with a cross. (b) A ‘model’ image constructed from a set of count rate scaled PSF subimages. A source mask, defined by the black contours, was produced by applying a cut at a surface brightness threshold of $0.01 \text{ pn+MOS ct ks}^{-1} \text{ pixel}^{-1}$. (c) The same X-ray image as shown in Panel (a) with the regions confused by bright sources masked out. The amplitude scaling is logarithmic with a dynamic range of 10. (d) The *GALEX* NUV (NUV: 2310 \AA) band image of M101 on the same spatial scale as the X-ray data. The scaling is logarithmic with a dynamic range of 10. In all four panels, the two large circles have radii of 5 and 10 arcmin.

and hard (2–6 keV). In each case, the pixel size was set at $4.35 \times 4.35 \text{ arcsec}^2$. The pn, MOS 1 and MOS 2 images in each of the three bands were first flat-fielded by subtracting a constant (non-vignetted) background particle rate (estimated from the count rates recorded in the corners of the CCD detectors not exposed to the sky) and then dividing by the appropriate exposure map. In the same process, bad pixels, hot columns and spurious data along chip gaps were excised. The resulting data from the three observations were then mosaicked into flat-fielded pn and MOS (MOS 1 plus MOS 2) images for each band. Since the medium- and hard-band images showed no evidence for diffuse emission, here we focus primarily on the images obtained in the soft (0.3–1 keV) band. Fig. 1(a) shows an adaptively smoothed soft-band image, obtained from the combined pn and MOS data sets, encompassing the central 20 arcmin diameter region centred on the optical nucleus of M101 (RA $14^{\text{h}}3^{\text{m}}12^{\text{s}}.55$, Dec. $+54^{\circ}20'56''.5$). The

amplitude scaling is logarithmic and adjusted so as to highlight the extended low surface brightness emission in M101.

To facilitate the investigation of the contribution of bright sources to the total X-ray emission in M101, a master source list, applicable to the three observations, was created. To this end, each of the new observations was analysed in turn using the source detection procedure described in Paper II (applied to the soft-, medium- and hard-band data). Then, by comparing the resulting source lists, the 108 sources detected in Observation 1 (Paper II) were supplemented by 21 new sources from Observation 2 and an additional nine new sources from Observation 3, to give a combined source catalogue of 138 sources (see the Appendix for details of the new sources).

The next step involved the construction of a spatial mask for the suppression of the bright X-ray sources in the central field of M101. Using the pn+MOS flat-fielded soft-band image, a soft-band source

count rate, net of the local background (LBG), was determined at each source position; in practice, we extracted the count rate within a cell of 16 arcsec radius centred on the source position, subtracted the LBG and lastly applied a correction for the extent of the point spread function (PSF) beyond the source cell. We then selected the sources within 11 arcmin radius of the nucleus of M101 with count rates above $1.5 \text{ pn+MOS ct ks}^{-1}$ as a ‘bright source sample’ to be excised from the soft-band image. Here, our approach was to construct a model image in which each source in our bright source list was represented by a PSF subimage centred on the source position and an intensity scaling commensurate with the measured source count rate. Then, by applying a cut at a surface brightness threshold of $0.01 \text{ pn+MOS ct ks}^{-1} \text{ pixel}^{-1}$, we were able to construct a bright source mask (see Fig. 1b). A total of 65 bright soft-band sources were removed within a radius of 11 arcmin of the nucleus of M101 (25 sources within 5 arcmin).

Fig. 1(c) shows the pn+MOS soft-band image of M101 after applying the bright source mask with the colour table adjusted to highlight the distribution of the residual emission.¹

The residual component is most prominent within the central 5 arcmin radius region, although it can be traced out to 10 arcmin in the radial profile distribution shown in Fig. 2. There is a clear correlation with the spiral structure of the galaxy, as is evident from a comparison with the *GALEX* near-UV (NUV; 2310 Å) band image of M101 (Bianchi et al. 2005; Popescu et al. 2005) shown in Fig. 1(d).

2.2 Spectral extraction of the diffuse component

The images in Fig. 1 demonstrate the existence of an extensive residual component in the soft X-ray emission of M101. In order to investigate the spectral properties of this component, we have extracted spectral data for the 5 arcmin radius region, centred on the position of the nucleus. A total of nine individual diffuse emission spectra were derived from the appropriate event files (for the three EPIC instruments, over the three observations). In each case, regions around bright point sources were excluded using the mask described earlier. (In practice, this involved the use of circular exclusion cells of radius 12–53 arcsec, as an approximation to the source mask used in the image analysis.)

Given the extended nature of the diffuse emission, the background subtraction is more complicated than is usual with EPIC data. The use of other *XMM-Newton* data sets deriving from ‘blank-field’ observations is, in our view, not a good option due to the variation from field to field in the soft X-ray background from the sky – clearly an important consideration when attempting to measure a soft diffuse signal. Instead LBG spectra were extracted from each event file for the annular region from 5 to 10 arcmin radius (see Fig. 1a) – again with the regions around bright sources excluded. We also extracted particle background (PBG) spectra from the out-of-field-of-view corner regions in each EPIC camera. The true background beneath the residual M101 emission in the central source region will be made up primarily of (vignetted) photons from the X-ray sky and (non-vignetted) particles, which comprise the instrumental background. The LBG spectra will also have photon and particle components,

¹ Hereafter, in this paper we use the word ‘residual’ to describe the X-ray emission of M101 after masking out the bright discrete X-ray sources. This residual component will include the truly diffuse emission, the integrated emission of discrete sources with count rates below our source-exclusion threshold and also some low-level contamination from bright sources due to the spillover beyond the masked regions of their extended PSFs (see Fig. 1b).

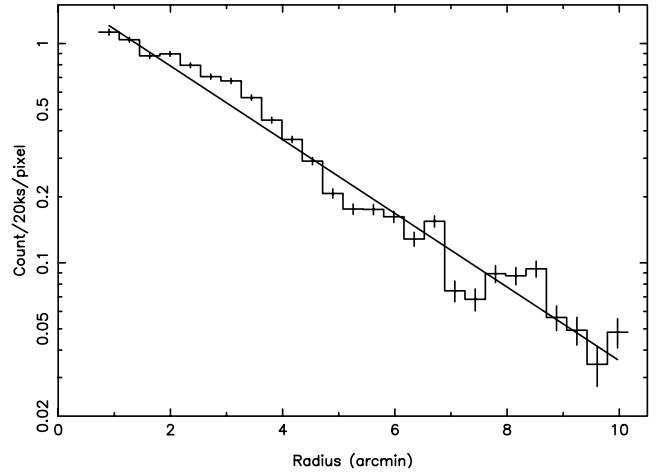


Figure 2. The radial distribution of the soft-band (0.3–1 keV) pn+MOS count rate. The sky background level has been subtracted. The solid line shows an exponential fall-off in the surface brightness with a scalelength of 2.6 arcmin (5.4 kpc), as determined from optical *B* data (Okamura, Kanazawa & Kodaira 1976).

but, as the LBG region is further off-axis than the source region, these components are not in the correct ratio for accurate background subtraction (since the signal reduction due to the vignetting is larger in the LBG region). However, a very good model of the true background can be made from a combination of the LBG and PBG spectra, provided the contributions of the two are appropriately scaled² to allow for the vignetting-corrected and actual areas of the central, LBG and PBG extraction regions. Using this approach, an appropriate composite background was determined for each central region spectrum together with the corresponding Redistribution Matrix File (RMF) and Auxiliary Response File (ARF) files. Finally for each data set, the spectral channels were binned together to give a minimum of 20 counts per bin.

Given the radial profile in Fig. 2, the above amounts to a differential measurement of the galaxy spectrum, which in effect compares the integrated signal in the central 5 arcmin region with the equivalent signal measured in the 5–10 arcmin annular region.

3 RESULTS

3.1 Luminosity and composition of the residual emission

After the exclusion of the bright source regions and subtracting the mean sky surface brightness measured in the 5–10 arcmin annulus, the count rate in the central 5 arcmin region is $0.28 \text{ pn+MOS ct s}^{-1}$ (0.3–1 keV). However, we need to apply three correction factors to obtain the ‘true’ central 5 arcmin count rate. The first accounts for the loss of ‘diffuse’ signal due to the source mask which blocks 12 per cent of the central area. The second factor allows for the differential nature of the measurement (i.e. the fact that we extract the background from the 5–10 arcmin annulus where the galaxy is still bright); on the basis of the radial profile determined earlier, we estimate that this effect suppresses the central count rate by

² The scale factors applied to the LBG and PBG spectra were, respectively, $(A_c/A_{\text{LBG}}) \times (V_c/V_{\text{LBG}})$ and $(A_c/A_{\text{PBG}}) \times (1 - V_c/V_{\text{LBG}})$. Here, A_c , A_{LBG} and A_{PBG} refer to the actual areas on the detector of the central, LBG and PBG extraction regions. Similarly, V_c and V_{LBG} are the average vignetting factors within the central and LBG regions.

≈ 19 per cent. Finally, the spillage of the bright source signal beyond the masked region (due to the extended PSF) contributes about 9 per cent of the measured residual count rate [as determined from the source model image shown in Fig. 1(b)]. The correction of all the three effects translates to a 28 per cent upward scaling of the residual count rate. If we adopt the best-fitting two-temperature model described in Section 3.2, the count rate to flux conversion factor is $1 \text{ pn+MOS ct s}^{-1} = 0.97 \times 10^{-12} \text{ erg cm}^{-2} \text{ s}^{-1}$ for the 0.5–2.0 keV band (fluxes corrected for Galactic absorption). The equivalent factors for the 0.3–1 and 0.45–1 keV bands are 1.16 and $0.91 \times 10^{-12} \text{ erg cm}^{-2} \text{ s}^{-1} (\text{ct s}^{-1})^{-1}$, respectively.

The implied luminosity of the central emission of M101 after excluding bright sources is $2.1 \times 10^{39} \text{ erg s}^{-1}$ in the 0.5–2 keV band. However, we must take into account the fact that our source exclusion threshold is relatively high [roughly a factor of 10 higher than that employed in the equivalent *Chandra* study (Kuntz et al. 2003)]. *Chandra* has shown that the $\log N - \log S$ relation for relatively faint sources in the central region of M101 (after correction for background AGNs) is quite flat with a slope of -0.80 ± 0.05 in the integral counts (Pence et al. 2001), implying that bright sources provide the dominant contribution to the discrete source luminosity of the galaxy. Using the count rate to flux conversion factor quoted earlier, our source exclusion threshold of $1.5 \text{ pn+MOS ct ks}^{-1}$ (0.3–1 keV) corresponds to a source luminosity of $9 \times 10^{36} \text{ erg s}^{-1}$ (0.5–2 keV), although this could be an underestimate for the harder spectral forms more typical of bright X-ray binaries. In fact, a source exclusion threshold of $1 \times 10^{37} \text{ erg s}^{-1}$ appears to be a reasonable estimate based on the average count rate to flux conversion obtained when we compare our measurements with those quoted in Pence et al. (2001) for the subset of common sources. As a check, at the latter luminosity threshold the *Chandra* source counts predict ≈ 25 sources within a central 5 arcmin region, which is very consistent with the number of sources actually excluded in our study. Using the *Chandra* source counts, we find the integrated luminosity in discrete sources from our exclusion cut-off down to a factor of 10 deeper (in effect the *Chandra* limit) amounts to about 20 per cent of the residual signal measured by *XMM–Newton*. In other words, our estimate of the ‘diffuse’ luminosity of M101 (after allowing for the contribution of sources brighter than $\sim 10^{36} \text{ erg s}^{-1}$) is $1.7 \times 10^{39} \text{ erg s}^{-1}$ (0.5–2 keV) in good agreement with the value reported by Kuntz et al. (2003) based on *Chandra* measurements of the same region.

3.2 Spectral properties of the residual emission

The nine epic spectra were fitted simultaneously using a variety of spectral models, with identical model parameters applied to each of the data sets. Visual inspection of the spectra indicated almost no emission above ≈ 1.5 keV. No acceptable fit could be obtained using just a single hot plasma component. However, a good fit (reduced $\chi^2 = 0.87$ for 2986 degrees of freedom) was obtained with a model incorporating two thermal (solar abundance) Mekal components, with absorption attributable to the hydrogen column density of our Galaxy in the direction of M101 ($1.16 \times 10^{20} \text{ cm}^{-2}$; Dickey & Lockman 1990). The derived temperatures for the two components were $0.20^{+0.01}_{-0.01}$ and $0.68^{+0.06}_{-0.04}$ keV (90 per cent confidence limits assuming one interesting parameter). The data plus best-fitting two-temperature model are shown in Fig. 3. (In this figure, we show the averages of the three pn and the six MOS spectra for clarity of display; however, the spectral-fitting results quoted here pertain to the fits to the nine individual spectra.) The absorption-corrected flux in the 0.3–1 keV band derived from the spectral fits was 3.0

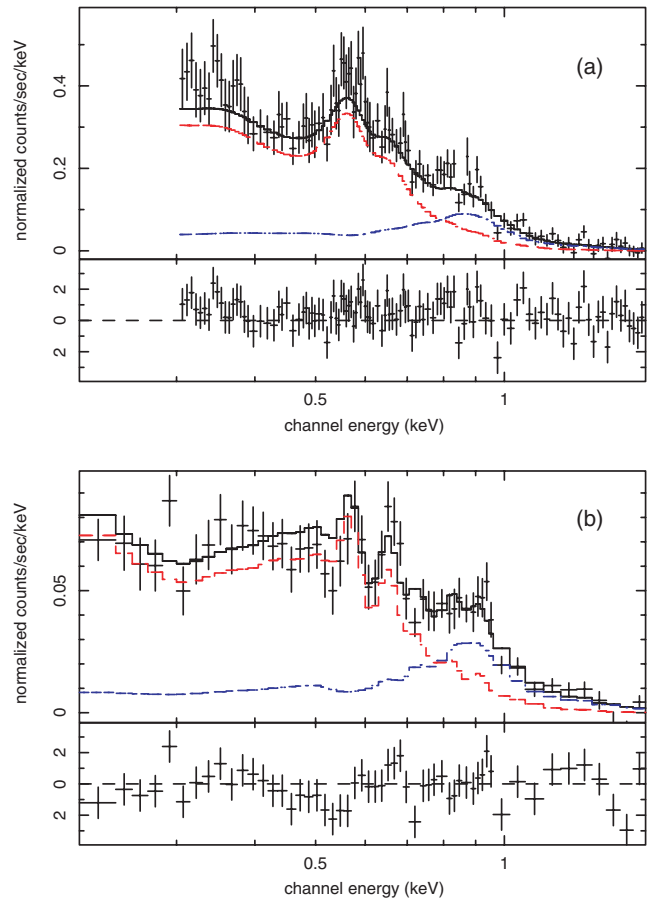


Figure 3. The EPIC spectra of the residual X-ray emission component in M101 after the exclusion of bright sources. (a) The pn spectrum averaged over the three observations. (b) The combined MOS spectrum averaged over the three observations. In both the cases, the solid line corresponds to the best-fitting two-component thermal spectrum with the dashed lines showing the individual contributions of the 0.2- and 0.7-keV components (see text). The χ^2 residuals with respect to the best-fitting model are also shown.

$\times 10^{-13} \text{ erg cm}^{-2} \text{ s}^{-1}$ of which the hotter component contributes 18 per cent. The corresponding values for the 0.5–2.0 keV band are $2.5 \times 10^{-13} \text{ erg cm}^{-2} \text{ s}^{-1}$ with the hotter component contributing 27 per cent. When we allowed the metallicity of the two plasmas to vary from unity (i.e. solar values), we obtained a best fit of 0.044 (0.038–0.055) solar for the lower temperature component and 0.17 (0.10–0.50) solar for the hotter component (with a reduced χ^2 for the fit of 0.81). However, this determination of strongly subsolar abundances is most probably an artefact of our attempt to fit relatively low spectral resolution data pertaining to a complex multiphase plasma with a simplistic spectral model, a problem which has in fact been well documented in the literature (e.g. Strickland et al. 2000; Wang et al. 2001). As noted by Kuntz et al. (2003), the abundances in the hot plasma in the central region of M101 are more likely to be near to solar rather than grossly subsolar.

We know that the measured *XMM–Newton* spectrum includes some residual contamination by the wings of the bright sources (estimated to be 9 per cent of the 0.3–1 keV count rate) and also includes a contribution from the underlying unresolved source population (estimated to contribute 20 per cent of the 0.5–2 keV flux). Since the sources may have somewhat harder spectra than the diffuse emission, presumably they contribute preferentially to the higher

temperature spectral component. However, our derived temperatures of ≈ 0.2 and ≈ 0.7 keV are in very good agreement with the results of Kuntz et al. (2003) based on *Chandra* observations, suggesting that some fraction of the harder emission does have a diffuse origin. In the following analysis, we assume 50 per cent of the measured hard emission is attributable to diffuse emission. We also scale the component normalizations obtained from the spectral fitting so as to correct for both the area of the source mask and the differential nature of the spectral measurement (as detailed in Section 3.1).

One can infer mean physical properties of the hot diffuse gas once some assumptions have been made regarding the geometry of the diffuse emission. Here, we assume that the gas is contained within a cylindrical region of radius of 10.5 kpc in the plane of the galaxy (matching a 5 arcmin angular extent) with a half-width perpendicular to the plane of 0.5 kpc (representing the extent of a putative shallow halo). Using this volume, the derived emission measure $\eta n_e^2 V$ (where η is the ‘filling factor’ – the fraction of the total volume V which is occupied by the emitting gas) can be used to infer the mean electron density n_e . For the 0.2 keV plasma, we find $n_e \approx 0.003 \eta^{-1/2} \text{ cm}^{-3}$ compared to a value of $\approx 0.001 \eta^{-1/2} \text{ cm}^{-3}$ for the 0.7 keV plasma, implying that these two components are in rough pressure balance. The thermal energy residing in each of the plasma components is comparable and totals $E_{\text{th}} \approx 6 \times 10^{55} \eta^{1/2} \text{ erg}$. The cooling is dominated by the line emission with radiative cooling

time-scales of $t_{\text{soft}} \approx 1.8 \times 10^8 \eta^{1/2} \text{ yr}$ and $t_{\text{hard}} \approx 1.5 \eta^{1/2} \text{ Gyr}$ for the cooler and hotter components, respectively.

3.3 Morphology of the residual emission

As previously noted, the spatial distribution of the residual soft X-ray emission in M101 shows a good correlation with the optical/UV emission of the galaxy, at least over the central 5 arcmin region. We have investigated this correlation using the FUV (1530 Å) and NUV (2310 Å) images of M101 from the *GALEX* pipeline (Morrissey et al. 2005), together with images recorded by the *XMM-Newton* Optical Monitor (OM) in the UVW1 ($\approx 2800 \text{ Å}$), *U*, *B* and *V* filters (Mason et al. 2001). The latter were derived from data taken during Observation 1 (UVW1) and Observation 3 (*U*, *B*, *V*) and subject to the standard SAS pipeline processing.

To aid the comparison, the soft X-ray image of Fig. 1(c) was compressed in both coordinates by a factor of 4 (to give $17.4 \times 17.4 \text{ arcsec}^2 \text{ pixel}$) and then lightly smoothed. The UV and optical images were first rebinned into the same image format as the original soft X-ray data, blurred by a mask representative of the on-axis *XMM-Newton* soft X-ray PSF and then further compressed in an identical way to the soft X-ray data.

Fig. 4 shows a detailed comparison of the 0.3–1 keV surface brightness measured in the central 5 arcmin radius region of M101

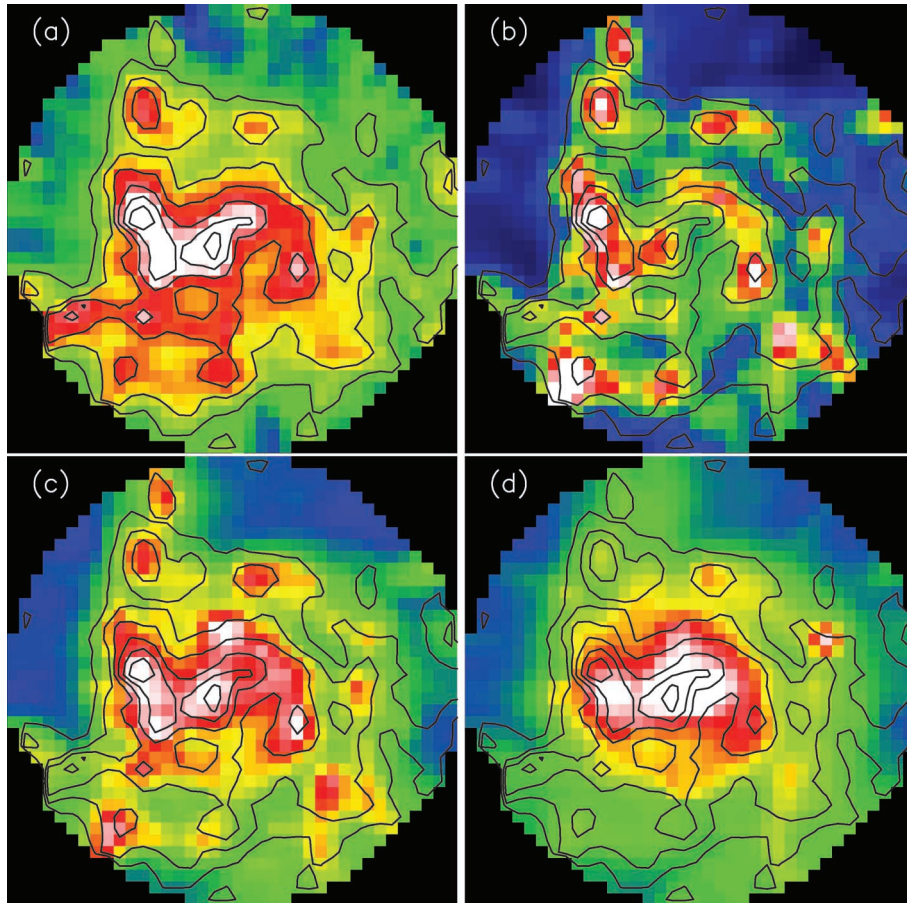


Figure 4. (a) The pn+MOS soft-band (0.3–1 keV) image of the central 5 arcmin radius region of M101. The scaling is linear. The contour levels increase in steps of $0.3 \text{ pn+MOS ct ks}^{-1} \text{ pixel}^{-1}$ from a starting level of $0.9 \text{ pn+MOS ct ks}^{-1} \text{ pixel}^{-1}$. (b) The *GALEX* NUV image of the same region overlaid with the soft X-ray contours. The scaling is linear in count pixel^{-1} units. (c) The *XMM-Newton* OM *U* image of the same region overlaid with the soft X-ray contours. The scaling is linear in count pixel^{-1} units. (d) The *XMM-Newton* OM *V* image of the same region overlaid with the soft X-ray contours. The scaling is linear in count pixel^{-1} units.

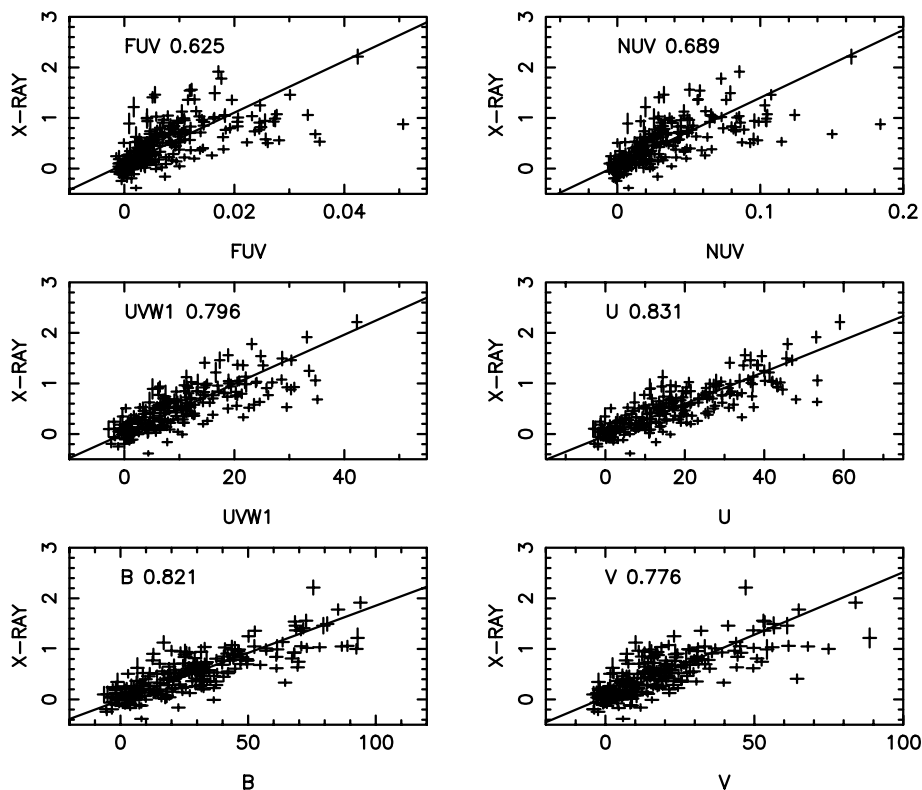


Figure 5. The correlation of the surface brightness measured in the soft X-ray band with that measured in other wavebands from the FUV through to V. The units in all cases are effectively counts per pixel. The numerical values quoted in each panel are the Pearson product moment correlation coefficient.

with the corresponding NUV, U - and V -band images. A striking similarity between the soft X-ray and U -band images is immediately obvious. In particular, the ‘S-feature’ which delineates the inner spiral structure of M101 is very prominent in both cases. The fall-off in the surface brightness towards the edges of the 5 arcmin field is also very similar in both wavebands, with the north–south asymmetry, evident at the level of the lowest soft X-ray contour level, also present in the U -band image. Interestingly, the correspondence becomes slightly less strong when the soft X-ray image is compared to both the NUV and V -band images. The NUV image is clearly totally dominated by bright H II regions and young star associations which together delineate the spiral arms of the galaxy, whereas in the soft X-ray image the general rise in surface brightness towards the nucleus has more relative impact. It would seem highly unlikely that these morphological trends could be induced by the increase in extinction as we move from the U band into the NUV. In contrast, comparison with the V -band data veers in the other direction with the soft X-ray image showing more structure outside the central 2 arcmin zone than the optical image.

The above trends are further illustrated in Fig. 5 which shows the pixel-by-pixel correlation between the soft X-ray surface brightness and the optical/UV surface brightness in the various wavebands. (Here, we use unsmoothed data with a pixel size of 34.8×34.8 arcsec², i.e. a factor of 8 compression of the original images.) The correlation, as measured by the Pearson product moment correlation coefficient, R , is at a maximum in the U band.

4 DISCUSSION

After excluding bright point sources (with $L_X > 10^{37}$ erg s^{−1}), we measure the residual soft X-ray luminosity of the inner (10.5 kpc

radius) disc of M101 to be $L_X \approx 2.1 \times 10^{39}$ erg s^{−1} (0.5–2 keV). Up to 20 per cent of this flux may originate in relatively bright point X-ray sources (with L_X down to 10^{36} erg s^{−1}), which remain unresolved in the XMM-Newton observations. A further 5 per cent of the measured luminosity may be attributable to intermediate luminosity sources (with L_X down to 10^{34} erg s^{−1}) and, at very faint levels, the integrated emission of dwarf stars may account for another 10 per cent contribution (Kuntz et al. 2003). Nevertheless, it seems that the bulk of observed X-ray emission is likely to be diffuse in origin.

The EPIC spectrum of the residual emission can be modelled as the sum of two thermal plasma components at temperatures of ≈ 0.2 and ≈ 0.7 keV with the harder component contributing 27 per cent of the flux in the 0.5–2 keV band (18 per cent in the 0.3–1 keV band). These spectral characteristics appear to be quite typical of the diffuse components seen in normal and starburst galaxies (e.g. Fraternali et al. 2002; Jenkins et al. 2004b,a) and, albeit with some caveats, consistent with spectral measurements for M101 reported in the literature (Snowden & Pietsch 1995; Wang 1999; Kuntz et al. 2003).

Earlier studies have demonstrated that for normal spiral galaxies, the total soft X-ray luminosity correlates with the total infrared luminosity (Read & Ponman 2001; Strickland et al. 2004a,b), the latter serving as a direct indicator of the current star formation rate. For the diffuse X-ray components, this is in line with the mechanism whereby the mechanical energy input from supernovae and the winds from young massive stars serves to heat the galactic ISM to million-degree temperatures. In the case of M101, the required rate of energy input is readily supplied by two supernovae per century (Matonick & Fesen 1997), if the efficiency of the conversion of the mechanical energy of the supernova explosion into X-rays is $10^{51}/E$ per cent, where E is the energy of the supernova in erg.

The linkage of X-ray emission to recent star formation is further strengthened by the finding that in a number of galaxies the X-ray morphology in the spiral arms matches that seen in the mid-infrared or $H\alpha$ (Tyler et al. 2004). A recent *Chandra* study has demonstrated that, in M101, the diffuse X-ray emission traces the spiral arms and is correlated with both the $H\alpha$ and FUV emission (Kuntz et al. 2003). In the same study, there was no evidence for any significant trend of X-ray spectral hardness with radius³ implying that the 0.2- and 0.7-keV spectral components are closely linked with one another and are both associated with star formation.

In the present paper, we have investigated this correlation in more detail by contrasting the X-ray morphology with that observed in FUV through to V band. We find that the correlation with the X-ray morphology is quite strong for all bands considered (FUV, NUV, UVW1, *U*, *B* and *V*), although the best match is obtained with the *U*-band data. One interpretation of this result is that, in broad terms, there are two underlying components present in the X-ray surface brightness distribution, namely a smooth rise towards the centre of the galaxy as reflected in the radial profile of the emission (Fig. 2) plus a superimposed X-ray spiral arm structure. In moving from the FUV through to the *V* band, clearly the balance shifts between the extreme Population I components (distributed in the spiral arms) and a more intermediate population (associated with the galactic disc) and it is in the *U* band that this balance happens to best match the X-ray morphology.

In the discs of spiral galaxies, star formation is thought to be triggered by the passage of a spiral density wave through the ISM. The formation of massive young stars results in a large UV/FUV flux with reprocessing in the immediate environment subsequently giving rise to associated $H\alpha$ and mid-IR emission. All of these serve as tracers of the spiral arms of the galaxy. Population synthesis models predict that following a star-formation burst, the peak in the UV/ $H\alpha$ production will last $\sim 3 \times 10^6$ yr, whilst the most massive stars complete their life cycle. The rate of energy deposition into the ISM from the subsequent supernovae rises at this time and remains fairly constant for $\sim 3 \times 10^7$ yr (Leitherer & Heckman 1995; Cervino, Mas-Hesse & Kunth 2002). Given the lag between the peak in UV/ $H\alpha$ emission and the X-ray heating, one might predict a spatial offset between the diffuse X-ray emission and the other spiral tracers, although as yet there is no clear observational evidence for such an effect (Tyler et al. 2004).

In the case of M101, we assume a flat rotation curve beyond a few kpc of the galaxy centre and a rotational velocity $v_{\text{rot}} \approx 200 \text{ km s}^{-1}$ (Bosma, Goss & Allen 1981). We further assume that the spiral pattern corotates with the disc material at three radial scalelengths, i.e. at $r \approx 15$ kpc. Then at $r \approx 7.5$ kpc a delay of 3×10^7 yr translates to a rotational lag of 24° or about 3 kpc in a direction perpendicular to the spiral arm. The effective pixel size in our multiwaveband correlation is 35 arcsec or 1.2 kpc, implying that a delay in the X-ray production following the passage of a spiral density wave might just be measurable in the current data. Unfortunately, the restricted signal-to-noise ratio and limited clarity of the spiral arm features in the X-ray image mitigates against the detection of

such an effect. Earlier we estimated a radiative cooling time-scale for the more prominent 0.2-keV plasma component to be $t_{\text{soft}} \approx 1.8 \times 10^8$ yr for a filling factor of $\eta \sim 1$. Clearly, this time-scale is inconsistent with the presence of reasonably narrow spiral features in the soft X-ray image. A very small filling factor, e.g. $\eta \sim 0.01$, is required to match the properties of X-ray spiral arms in M101, suggesting a very clumpy thin-disc distribution. In fact, a reasonable scenario is that the spiral arms in X-rays are delineated by a combination of truly diffuse emission, possibly in the form of hot gas bubbles and superbubbles, plus contributions from individual SNRs and concentrations of unresolved discrete sources. As noted by Kuntz et al. (2003), the available constraints suggest that superbubbles in the disc of M101 may have similar properties to the Galactic Loop I superbubble (Egger & Aschenbach 1995), although they are not individually resolvable even in *Chandra* data. Where there is no confinement by chimneys or similar structures in the ISM, energy losses arising from adiabatic expansion of the hot gas in the disc into the lower halo of M101 may also help localize the spiral arm component [in M101 the sound speed of the soft component is comparable to the escape velocity from the disc (Kuntz et al. 2003)].

The second spatial component of the X-ray emission considered above broadly follows the distribution of the optical light attributable to the intermediate disc stellar population. The integrated X-ray emission of dwarf stars will presumably follow a disc distribution but this is unlikely to represent a substantial contribution [10 per cent overall in the 0.5–2 keV band but, given the typical $kT \sim 0.8$ keV temperature of dwarf-star coronae, falling to ≈ 5 per cent in the softer 0.3–1 keV band (Kuntz et al. 2003)]. Other contributions to this smoother distribution might be expected from supernovae in the interarm regions associated with disc population stars and X-ray emitting gas which has accumulated in a shallow halo in M101 as a result of galactic chimney/fountain activity. In the case of the latter, gas which has cooled substantially due to adiabatic expansion may, as a result of a frozen-in non-ionization equilibrium, exhibit an emission spectrum dominated by oxygen lines, which mimics that expected from a 0.2 keV plasma (Breitschwerdt & Schmutzler 1999). The fact that the X-ray surface brightness increases towards the centre of M101 is most naturally explained in terms of an increase in activity per unit disc area, with the filling factor of the extended z -height component possibly approaching unity near the centre of the galaxy. With the latter assumption, the implied electron density and pressure in the inner halo of M101 are comparable to that inferred for the centre of Galactic Loop I and the Local Hot Bubble.

5 CONCLUSIONS

This is the third and final paper in a series presenting the results of *XMM-Newton* observations of the nearby face-on Scd spiral galaxy M101. Here, we focus on the spatial and spectral properties of the galaxy, when bright X-ray sources with $L_X > 10^{37} \text{ erg s}^{-1}$ are removed using an appropriate point source mask.

The residual soft X-ray luminosity of the central (10.5 kpc radius) region of M101 was measured as $L_X \approx 2.1 \times 10^{39} \text{ erg s}^{-1}$ (0.5–2 keV), the bulk of which appears to originate as diffuse emission. We find a two-temperature model best fits the spectral data with the derived temperatures of $0.20 \pm 0.01 \text{ keV}$ and $0.68^{+0.06}_{-0.04} \text{ keV}$, typical of the diffuse components seen in other normal and starburst galaxies.

In line with earlier studies, we find that the observed X-ray surface brightness distribution is well correlated with images recorded in optical/UV wavebands. In particular, the detection of spiral arms in

³ We have subsequently checked the *XMM-Newton* data for spectral trends by extracting images in the 0.3–0.8 and 0.8–1.2 keV subbands. The radial profiles of the residual X-ray emission in these subbands are consistent with the results obtained for the broader 0.3–1.0 keV band (see Fig. 2) and within the errors, exhibit a constant ratio for radii in the range 1–10 arcmin. The *XMM-Newton* observations thus confirm that there is no significant radial dependence of spectral hardness in this Galaxy.

X-rays establishes a close link between the X-ray emission and recent star formation. Closer investigation suggests that the X-ray morphology may comprise both a spiral arm component and a smoother disc component. In spiral galaxies, star formation is thought to be triggered by the passage of a spiral density wave through the ISM. In principle, one might observe a lag between more immediate star formation indicators such as the UV/FUV flux or H α and the heating of the ISM to X-ray temperatures as a result of subsequent supernova. The XMM–Newton data show no evidence for such an effect but it may be observable in future high-resolution and high signal-to-noise data. Whereas the spiral arm component, on the basis of the radiative cooling time-scale of the 0.2-keV plasma, may be deduced to have a clumpy, low- z distribution, the smoother disc component may represent longer lived X-ray gas with a relatively large filling factor, which has been transported to the lower halo of M101 via the galactic chimney/fountain mechanism.

Future progress in understanding the X-ray properties of normal spiral galaxies will no doubt follow from very intensive studies of individual galaxies [e.g. the recent 1 Ms observation of M101 with *Chandra* (Kuntz et al. in preparation)] and by applying appropriately optimised analysis procedures to samples of nearby galaxies, as is now possible using archival data sets.

ACKNOWLEDGMENTS

LPJ, TPR and RAO acknowledge PPARC support at various junctures during this project. We should also like to thank the anonymous referee for some helpful comments and suggestions.

REFERENCES

- Bianchi L. et al., 2005, *ApJ*, 619, L71
 Bosma A., Goss W. M., Allen R. J., 1981, *A&A*, 93, 106
 Bregman J. N., 1980, *ApJ*, 236, 577
 Bregman J. N., Glassgold A. E., 1982, *ApJ*, 263, 564
 Breitschwerdt D., Schmutzler T., 1999, *A&A*, 347, 650
 Cervino M., Mas-Hesse J. M., Kunth D., 2002, *A&A*, 392, 19
 Cui W., Sanders W. T., McCammon D., Snowden S. L., Womble D. S., 1996, *ApJ*, 468, 102
 de Vaucouleurs G., de Vaucouleurs A., Corwin H. G., Buta R. J., Paturel G., Fouque P., 1991, *Third Reference Catalogue of Bright Galaxies*. Springer-Verlag, Berlin
 Dickey J. M., Lockman F. J., 1990, *ARA&A*, 28, 215
 Egger R., Aschenbach B., 1995, *A&A*, 1995, 294, L25
 Fraternali F., Cappi M., Sancisi R., Osterloo T., 2002, *ApJ*, 578, 109
 Heckman T. M., Armus L., Miley G. K., 1990, *ApJS*, 74, 833
 Jenkins L. P., Roberts T. P., Warwick R. S., Kilgard R. E., Ward M. J., 2004b, *MNRAS*, 349, 404 (Paper I)
 Jenkins L. P., Roberts T. P., Ward M. J., Zezas A., 2004b, *MNRAS*, 352, 1335
 Jenkins L. P., Roberts T. P., Ward M. J., Zezas A., 2005a, *MNRAS*, 357, 109
 Jenkins L. P., Roberts T. P., Warwick R. S., Kilgard R. E., Ward M. J., 2005b, *MNRAS*, 357, 401 (Paper II)

- Kong A. K. H., Di Stefano R., Yuan F., 2004, *ApJ*, 617, L49
 Kuntz K. D., Snowden S. L., Pence W. D., Mukai K., 2003, *ApJ*, 588, 264
 Martin C. L., Kobulnicky H. A., Heckman T. M., 2002, *ApJ*, 574, 663
 Leitherer C., Heckman T. M., 1995, *ApJS*, 96, 9
 Mason K. O. et al., 2001, *A&A*, 365, L36
 Matonick D. M., Fesen R. A., 1997, *ApJS*, 112, 49
 McCammon D., Sanders W. T., 1984, *ApJ*, 287, 167
 Morrissey P. et al., 2005, *ApJ*, 619, L7
 Mukai K., Pence W. D., Snowden S. L., Kuntz K. D., 2003, *ApJ*, 582, 184
 Mukai K., Still M., Corbet R. H. D., Kuntz K. D., Barnard R., 2005, *ApJ*, 634, 1085
 Norman C. A., Ikeuchi S., 1989, *ApJ*, 345, 372
 Okamura S., Kanazawa T., Kodaira K., 1976, *PASJ*, 28, 329
 Pence W. D., Snowden S. L., Mukai K., Kuntz K. D., 2001, *ApJ*, 561, 189
 Pietsch W. et al., 2001, *A&A*, 365, L174
 Popescu C. C. et al., 2005, *ApJ*, 619, L75
 Read A. M., Ponman T. J., Strickland D. K., 1997, *MNRAS*, 286, 626
 Read A. M., Ponman T. J., 2001, *MNRAS*, 328, 127
 Shapiro P. R., Field G. B., 1976, *ApJ*, 205, 762
 Snowden S. L., Pietsch W., 1995, *ApJ*, 452, 627
 Stetson P. B. et al., 1998, *ApJ*, 508, 491
 Stevens I. R., Read A. M., Bravo-Guerrero J., 2003, *MNRAS*, 343, L47
 Strickland D. K., Heckman T. M., Weaver K. A., Dahlem M., 2000, *AJ*, 120, 2965
 Strickland D. K., Heckman T. M., Colbert E. J. M., Hoopes C. G., Weaver K. A., 2004a, *ApJS*, 151, 193
 Strickland D. K., Heckman T. M., Colbert E. J. M., Hoopes C. G., Weaver K. A., 2004b, *ApJ*, 606, 829
 Trinchieri G., Fabbiano G., Romaine S., 1990, *ApJ*, 356, 110
 Tyler K., Quillen A. C., LaPage A., Rieke G. H., 2004, *ApJ*, 610, 213
 Wang Q. D., 1999, *ApJ*, 517, L27
 Wang Q. D., Immler S., Pietsch W., 1999, *ApJ*, 523, 121
 Wang Q. D., Immler S., Walterbos R., Lauroesch J. T., Breitschwerdt D., 2001, *ApJ*, 555, L99
 Watson M. G., Stanger V., Griffiths R. E., 1984, *ApJ*, 286, 144

APPENDIX A: THE POINT SOURCE CATALOGUE

Within the D₂₅ circle of M101, 108 sources were detected in Observation 1, 91 in Observation 2 and the same number in Observation 3. Ninety sources were detected in at least two of the observations. For completeness, Table A1 lists the additional 21 sources detected in Observation 2 and another 9 sources detected in Observation 3. The format of the table is identical to that of table 1 of Paper II and the numbering scheme is a continuation of the original list of 108 sources.

The most notable new source to appear in the second and third observations is source no. 122, which corresponds to the supersoft transient P98 (Mukai et al. 2003). The results from the XMM–Newton and *Chandra* observations of this object are reported in Kong et al. (2004) and Mukai et al. (2005).

This paper has been typeset from a \LaTeX file prepared by the author.

Table A1. Additional sources detected within the D_{25} circle of M101 in Observations 2 (109–129) and 3 (130–138).

Src	XMMU	$r_{1\sigma}$ (arcsec)	S	pn count rate (count ks ⁻¹) M (4)	H	MOS count rate (count ks ⁻¹) S (5)	M	H	F_X	L_X	HR1	HR2
(1)	(2)	(3)							(6)	(7)	(8)	(9)
109	J140213.8+542158	1.95	3.1 ± 0.9	0.1 ± 0.3	1.7 ± 0.8	0.8 ± 0.2	0.9 ± 0.2	0.7 ± 0.2	1.58 ± 0.27	0.98 ± 0.17	-0.47 ± 0.12	0.21 ± 0.16
110	J140237.7+542733	2.98	-	-	-	0.4 ± 0.2	0.9 ± 0.2	0.3 ± 0.2	0.90 ± 0.30	0.56 ± 0.19	0.41 ± 0.24	-0.52 ± 0.28
111	J140238.0+541215	2.31	-	-	-	0.5 ± 0.2	1.0 ± 0.3	0.3 ± 0.2	1.11 ± 0.32	0.69 ± 0.20	0.34 ± 0.21	-0.49 ± 0.26
112	J140246.7+541454	2.01	0.0 ± 0.3	2.8 ± 0.6	1.3 ± 0.5	0.0 ± 0.1	0.7 ± 0.2	0.4 ± 0.2	1.00 ± 0.21	0.62 ± 0.13	1.00 ± 0.14	-0.32 ± 0.15
113	J140251.4+540901	2.93	-	-	-	1.2 ± 0.3	1.2 ± 0.3	0.4 ± 0.2	1.56 ± 0.39	0.97 ± 0.24	0.00 ± 0.18	-0.49 ± 0.26
114	J140257.9+542655	2.07	1.0 ± 0.4	1.4 ± 0.5	1.5 ± 0.5	0.2 ± 0.1	0.5 ± 0.2	0.8 ± 0.2	1.27 ± 0.22	0.79 ± 0.13	0.25 ± 0.20	0.16 ± 0.15
115	J140302.0+541336	2.00	1.8 ± 0.5	0.8 ± 0.4	0.0 ± 0.2	0.6 ± 0.2	0.2 ± 0.1	0.1 ± 0.1	0.40 ± 0.12	0.25 ± 0.08	-0.43 ± 0.17	-0.67 ± 0.41
116	J140304.0+541040	2.07	2.8 ± 0.8	1.2 ± 0.5	0.0 ± 0.4	0.5 ± 0.2	0.8 ± 0.2	0.1 ± 0.2	0.64 ± 0.18	0.39 ± 0.11	-0.07 ± 0.15	-0.76 ± 0.28
117	J140306.9+541007	2.28	-	-	-	0.3 ± 0.2	0.0 ± 0.1	1.2 ± 0.3	1.79 ± 0.47	1.11 ± 0.29	-1.00 ± 0.89	1.00 ± 0.22
118	J140308.3+543229	2.01	-	-	-	1.4 ± 0.3	0.0 ± 0.1	0.0 ± 0.0	0.60 ± 0.17	0.38 ± 0.10	-1.00 ± 0.13	0.00 ± 0.00
119	J140320.0+542034	2.93	-	-	-	0.7 ± 0.2	0.1 ± 0.1	0.0 ± 0.1	0.35 ± 0.14	0.22 ± 0.09	-0.70 ± 0.24	-1.00 ± 1.36
120	J140324.0+542336	2.58	2.5 ± 0.5	0.4 ± 0.3	0.0 ± 0.1	-	-	-	0.34 ± 0.11	0.21 ± 0.07	-0.75 ± 0.17	-0.83 ± 0.69
121	J140327.5+541909	1.82	2.1 ± 0.5	1.1 ± 0.3	0.8 ± 0.3	0.4 ± 0.1	0.5 ± 0.1	0.4 ± 0.1	0.88 ± 0.14	0.55 ± 0.09	-0.14 ± 0.14	-0.12 ± 0.16
122	J140332.4+542103	1.73	5.5 ± 0.7	0.1 ± 0.2	0.6 ± 0.3	0.9 ± 0.2	0.0 ± 0.0	0.0 ± 0.1	0.55 ± 0.10	0.34 ± 0.06	-0.98 ± 0.04	0.64 ± 0.45
123	J140334.3+540930	1.95	4.2 ± 0.9	2.7 ± 0.7	1.9 ± 0.8	1.0 ± 0.3	0.5 ± 0.2	0.9 ± 0.3	1.91 ± 0.32	1.19 ± 0.20	-0.26 ± 0.13	0.04 ± 0.17
124	J140354.1+541108	2.20	-	-	-	1.4 ± 0.3	0.0 ± 0.1	0.1 ± 0.2	0.79 ± 0.27	0.49 ± 0.17	-1.00 ± 0.17	1.00 ± 1.74
125	J140355.8+542100	1.68	6.3 ± 0.8	2.2 ± 0.5	0.7 ± 0.4	0.9 ± 0.2	0.7 ± 0.2	0.1 ± 0.1	1.03 ± 0.14	0.64 ± 0.09	-0.38 ± 0.08	-0.62 ± 0.16
126	J140357.2+541011	2.11	5.5 ± 1.1	2.3 ± 0.7	1.1 ± 0.7	0.6 ± 0.3	0.4 ± 0.3	1.0 ± 0.3	1.67 ± 0.32	1.03 ± 0.20	-0.38 ± 0.14	0.02 ± 0.21
127	J140401.2+542344	2.59	2.3 ± 0.5	0.0 ± 0.2	0.3 ± 0.4	-	-	-	0.44 ± 0.23	0.27 ± 0.14	-1.00 ± 0.16	1.00 ± 1.09
128	J140429.8+542235	2.19	-	-	-	0.3 ± 0.2	0.8 ± 0.2	0.6 ± 0.2	1.25 ± 0.30	0.78 ± 0.19	0.43 ± 0.23	-0.18 ± 0.22
129	J140435.4+542101	1.59	12.9 ± 1.3	0.0 ± 0.2	0.0 ± 0.2	-	-	-	1.41 ± 0.20	0.88 ± 0.12	-1.00 ± 0.03	-1.00 ± 1.00
130	J140429.9+542243	1.54	14.0 ± 1.4	0.0 ± 0.3	0.0 ± 0.4	-	-	-	1.44 ± 0.26	0.89 ± 0.16	-1.00 ± 0.04	0.00 ± 0.00
131	J140230.0+541611	2.05	3.6 ± 1.1	4.4 ± 1.0	3.2 ± 1.1	1.2 ± 0.3	1.2 ± 0.4	0.7 ± 0.4	2.30 ± 0.42	1.43 ± 0.26	0.07 ± 0.14	-0.20 ± 0.17
132	J140243.6+542007	2.38	2.1 ± 0.6	0.4 ± 0.3	0.4 ± 0.4	-	-	-	0.48 ± 0.24	0.30 ± 0.15	-0.70 ± 0.25	0.04 ± 0.71
133	J140250.7+542857	3.01	2.5 ± 0.7	0.0 ± 0.1	1.3 ± 0.7	-	-	-	1.00 ± 0.37	0.62 ± 0.23	-1.00 ± 0.09	1.00 ± 0.17
134	J140300.6+540958	2.24	4.3 ± 1.0	2.0 ± 0.7	1.0 ± 0.8	-	-	-	1.29 ± 0.45	0.80 ± 0.28	-0.36 ± 0.18	-0.36 ± 0.38
135	J140312.2+541754	2.19	3.8 ± 0.7	0.3 ± 0.3	0.1 ± 0.2	-	-	-	0.50 ± 0.14	0.31 ± 0.09	-0.84 ± 0.13	-0.45 ± 0.76
136	J140314.4+542132	2.79	-	-	-	0.6 ± 0.2	0.2 ± 0.1	0.2 ± 0.1	0.57 ± 0.19	0.35 ± 0.12	-0.49 ± 0.25	-0.15 ± 0.48
137	J140355.8+540856	2.10	4.0 ± 0.9	2.9 ± 0.8	1.3 ± 0.7	-	-	-	1.57 ± 0.44	0.97 ± 0.27	-0.17 ± 0.17	-0.39 ± 0.27
138	J140415.6+540948	1.75	7.2 ± 1.1	4.5 ± 0.9	1.5 ± 0.9	2.0 ± 0.4	1.0 ± 0.3	0.6 ± 0.3	2.12 ± 0.31	1.31 ± 0.19	-0.26 ± 0.09	-0.41 ± 0.17

(1) Source number; (2) XMMU source designation (J2000 coordinates); (3) 1σ error radius (including a 1.5 arcsec systematic error); (4 and 5) source count rates in soft (0.3–1 keV), medium (1–2 keV) and hard (2–6 keV) bands for the pn and MOS cameras, with the significant source detections ($> 4\sigma$) highlighted in bold; (6) source flux in units of 10^{-14} erg cm⁻² s⁻¹ in the broad (0.3–6 keV) band; (7) source luminosity in units of 10^{38} erg s⁻¹ in the 0.3–6 keV band (assuming a distance to M101 of 7.2 Mpc); (8 and 9) soft (HR1) and hard (HR2) hardness ratios.